From cyclic sand ratcheting to tilt accumulation of offshore monopiles
3D FE modelling using SANISAND-MS

Liu, H.Y.; Kementzetzidis, E.; Abell, J. A.; Pisano, F.

DOI
10.1680/jgeot.20.P.029

Publication date
2021

Document Version
Accepted author manuscript

Published in
Géotechnique

Géotechnique **00**, 1–17 [http://dx.doi.org/10.1680/geot.XX.XXXXX]

From cyclic sand ratcheting to tilt accumulation of offshore monopiles: 3D FE modelling using SANISAND-MS

H. Y. LIU*, E. KEMENTZETZIDIS‡, J. A. ABELL†, F. PISANÒ‡

Serviceability criteria for offshore monopiles include the estimation of long-term, permanent tilt under repeated operational loads. In the lack of well-established analysis methods, experimental and numerical research has been carried out in the last decade to support the fundamental understanding of monopile-soil interaction mechanisms, and the conception of engineering methods for monopile tilt predictions. With focus on the case of monopiles in sand, this work shows how step-by-step/implicit, three-dimensional finite element modelling can be fruitfully applied to the analysis of cyclic monopile-soil interaction and related soil deformation mechanisms. To achieve adequate simulation of cyclic sand ratcheting and densification around the pile, the SANISAND-MS model recently proposed by Liu *et al.* (2019b) is adopted. The link between local soil behaviour and global monopile response to cyclic loading is discussed through detailed analysis of model prediction. Overall, the results of numerical parametric studies confirm that the proposed 3D FE modelling framework can reproduce relevant experimental evidence about monopile-soil interaction, and support future improvement of engineering design methods.

KEYWORDS: offshore wind, monopile, cyclic loading, tilt, constitutive modelling, finite element modelling

INTRODUCTION

The offshore wind energy sector is rapidly expanding worldwide (Tsai *et al.*, 2016; Mattar & Borvarán, 2016; Archer *et al.*, 2017; Chancham *et al.*, 2017). Recent technological advances have supported the growth in size and power output of offshore wind turbines (OWTs), as well as the reduction of fabrication and installation costs. Moving towards deeper and harsher waters poses significant technical challenges, especially regarding support structures and foundations. At present, most OWTs are founded on monopiles, which are tubular steel piles of large diameter and low embedment ratio (embedded length/diameter, $\sim 3-6$). Due to the large costs for materials and installation, the optimisation of foundation design is key to cost-effective offshore wind developments.

Monopile design is mostly driven by the following criteria (Bhattacharya, 2019):

1. first resonance frequency of the turbine-foundation-soil system to lie within prescribed limits ('soft-stiff' range);
2. sufficient resistance to structural fatigue under prolonged operational loads;
3. sufficient capacity under loads of exceptional magnitude;
4. full serviceability, i.e. limited deformations, under any environmental and/or mechanical loads.

Regarding the fourth criterion, it is of special interest to avoid in the long term excessive accumulation of rotation/deflection under repeated loading. Specifically, some OWT manufacturers prescribe that permanent OWT-monopile tilt should not exceed $\sim 0.5^{\circ}$ over the whole operational life, also including some deviation from perfect verticality after installation (Arany *et al.*, 2015). In the lack of well-established calculation procedures, intensive work has been carried out to explain and quantify geotechnical mechanisms governing monopile tilt under lateral cyclic loading (Houlsby, 2016). The tilting response of monopile results overall from the interplay of several factors, such as loading conditions, soil type and behaviour, geometry and mechanical properties of the foundation.

Significant experimental work has been devoted in the last decade to the study of monopile tilt under high-cyclic lateral loading, mostly for the case of sandy soils under drained conditions (i.e., without accounting for pore pressure effects) – see the recent overviews provided, e.g., by Truong *et al.* (2019) and Page *et al.* (2020). As for numerical modelling research, the intrinsic complexity of the problem has promoted the development of simplified analysis methods. In particular, the following approaches for numerical tilt predictions have gained broadest popularity:

– methods based on '0D' modelling of monopile-soil interaction. In this approach, distributed/continuum geotechnical mechanisms are lumped into a single macro-element formulated in terms of only a few pairs

Manuscript received...
* Department of Offshore Energy - Advanced Modelling Section, Norwegian Geotechnical Institute, 0806, Oslo, Norway (formerly Delft University of Technology)
† Facultad de Ingeniería y Ciencias Aplicadas, Universidad de los Andes, Mons. Álvaro del Portillo 12.455, 762000111, Las Condes, Santiago, Chile
‡ Faculty of Civil Engineering and Geoscience, Delft University of Technology, Stevinweg 1, 2628 CN Delft, The Netherlands

(six at most) of generalised static (forces/moments) and kinematic (displacement/rotations) variables (Houlsby *et al.*, 2017; Abadie *et al.*, 2019b). Non-linear monopile macro-elements have also been used to account for soil-foundation interaction effects in the dynamic analysis of OWTs (Page *et al.*, 2019), and may potentially be extended to tackle cyclic loading conditions (di Prisco & Pisanò, 2011);

– methods based on 3D soil-foundation modelling and simulation of the 'local' soil response around the foundation. While space discretisation is usually performed through the finite element (FE) method, time marching can be tackled according to two distinct approaches – either 'explicit' or 'implicit', in the terminology used by Niemunis *et al.* (2005).

In the explicit framework, accumulated strains are explicitly linked to the number of loading cycles N, so that relevant components of accumulated strain are calculated at all soil locations only at one selected time for each loading cycle. Owing to their relatively low computational costs, explicit methods have been already applied by several authors to the 3D FE analysis of cyclically loaded monopiles (Achmus *et al.*, 2009; Jostad *et al.*, 2014; Wichtmann *et al.*, 2017; Chong, 2017; Staubach & Wichtmann, 2020). Explicit models rely on extensive laboratory testing programmes, and build on the translation of cyclic loading histories into sequences of N-driven monotonic steps. In contrast, the implicit approach is more 'conventional' in that it encompasses the simulation of cyclic soil behaviour as a causal sequence of stress/strain increments, to be integrated in the time domain (step-by-step integration). To date, 0D-implicit and 3D-explicit approaches have been preferred to implicit 3D simulations – so far only rarely applied to monopile tilt problems (Barari *et al.*, 2017; Sheil & McCabe, 2017). Nonetheless, implicit 3D FE modelling appears to possess higher potential to explain/predict governing geo-mechanisms (Pisanò, 2019; Jostad *et al.*, 2020; Liu, 2020; Cheng *et al.*, 2021), and is being increasingly adopted to study the cyclic/dynamic performance of OWT-monopile-soil systems (Cuéllar *et al.*, 2014; Kementzetzidis *et al.*, 2018, 2019, 2020). Furthermore, it is envisaged that implicit approaches may support in the near future the refinement of existing explicit models, for instance with regard to the cyclic evolution of phenomenological/non-measurable variables adopted in implicit constitutive models. The two approaches could eventually be combined to set a path from experimental observations to engineering predictions that passes through a stage of more detailed (implicit) modelling. Such a stage would allow the generalisation of laboratory data to conditions not directly tested, and ultimately the improvement of empirical/explicit laws.

At the present state of the art, performing sound 3D FE calculations is still challenging for the following reasons:

– cyclic deformations develop in the soil under the influence of numerous factors. The influence of the loading history and soil microstructure is by now well acknowledged (Park & Santamarina, 2019; Gao & Meguid, 2018)

– numerical approximation errors are inevitably produced during the time integration of stress/strain increments in each loading cycle. As a consequence, numerical errors might accumulate in the presence of a large number of cycles (Niemunis *et al.*, 2005), depending on the adopted stress point integration strategy;

– the need for accurate time integration over numerous loading cycles makes implicit 3D FE modelling computationally demanding. This issue is particularly apparent for OWT foundation problems, which can involve up to 10^7-10^8 operational cycles.

This study highlights the benefits of implicit 3D FE modelling in relation to the tilting analysis of monopiles in sand. Such a goal is pursued through the application of SANISAND-MS, a constitutive model recently proposed by Liu *et al.* (2019b) to enhance the simulation of high-cyclic sand ratcheting (Wichtmann, 2005; di Prisco & Mortara, 2013), and therefore the assessment of foundation serviceability under cyclic loading. Following recent constitutive modelling work (Liu *et al.*, 2019b; Liu & Pisanò, 2019; Liu *et al.*, 2020), SANISAND-MS is here adopted for the first time to tackle a 3D boundary value problem.

It is worth recalling that a thorough validation process should include quantitative comparison between the results of pile loading tests and corresponding 3D FE simulations, with the latter to be performed using soil parameters calibrated against soil laboratory data. However, the experimental literature does not yet sufficiently support to such endeavor, since it is still difficult to access pile test results obtained after thorough (high-)cyclic characterisation (Truong *et al.*, 2019; Richards *et al.*, 2019). Therefore, an alternative approach was followed to achieve a semi-quantitative validation of the considered framework. 3D FE simulations of an average' full-scale monopile were performed by using SANISAND-MS parameters identified by Liu *et al.* (2019b) for a sand extensively tested in Karlsruhe (Wichtmann, 2005). After detailed inspection of the numerical results, simulated trends of cyclic monopile tilt were semi-quantitatively' compared to experimental data from the literature. As a first take on the subject, the scope of this paper is limited to the case of a monopile wished-in-place' in dry sand and subjected to unidirectional lateral loading, with emphasis on the interplay of cyclic loading and sand density conditions in determining the permanent tilt of the reference monopile.

SANISAND-MS MODEL

This section summarises key aspects of the SANISAND-MS model, which was recently proposed to improve the simulation of cyclic sand behaviour (Liu *et al.*, 2019b; Liu & Pisanò, 2019) with regard to drained high-cyclic ratcheting and related strain accumulation (Wichtmann, 2005). As this paper exclusively addresses the case of a monopile in dry sand, the application of SANISAND-MS to hydro-mechanical coupled problems was not attempted, although recently tackled from a constitutive modelling perspective (Liu *et al.*, 2018, 2019a, 2020).

SANISAND-MS' bounding surface formulation builds on the parent SANISAND2004 model developed by Dafalias & Manzari (2004), with the addition of a so-called 'memory surface' in replacement of the fabric tensor (Corti *et al.*, 2016).

The model adopts a critical state framework with four relevant loci (Fig. 1): (1) a narrow conical yield locus (f), enclosing the elastic domain; (2) a wide conical bounding surface (f^B), setting current stress bounds consistent with an evolving state parameter (Been & Jefferies, 1985), as proposed by Manzari & Dafalias (1997); (3) a conical dilatancy surface (f^D), separating stress zones associated with contractive and dilative deformations (Manzari & Dafalias, 1997; Li & Dafalias, 2000; Dafalias & Manzari, 2004); (4) a conical memory surface (f^M), bounding an evolving stress region associated with non-virgin loading, and therefore related to the evolution of stress-induced anisotropy at the micro-scale. The memory surface allows a phenomenological representation of micro-mechanical effects associated with fabric changes occurring during cycling, such as variations in stiffness and dilatancy. Such changes possess at the micro-scale both intensity' and directionality' attributes, which inspired the introduction in SANISAND-MS of a combined isotropic-kinematic hardening mechanism for the memory surface (Corti *et al.*, 2016; Liu *et al.*, 2019b).

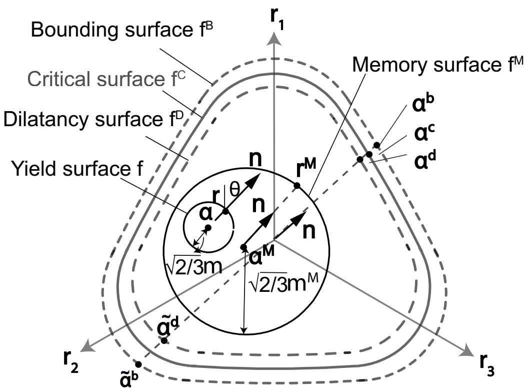

Fig. 1. SANISAND-MS model loci in the deviatoric stress ratio plane.

The evolution of elasto-plastic sand stiffness is governed in SANISAND-MS both by the bounding and the memory surfaces through the plastic modulus K_p:

$$K_p = \frac{2}{3} ph(\boldsymbol{\alpha}^b - \boldsymbol{\alpha}) : \boldsymbol{n} \tag{1}$$

where $(\boldsymbol{\alpha}^b - \boldsymbol{\alpha}) : \boldsymbol{n}$ quantifies the distance between the back-stresses associated with bounding and yield surfaces ($\boldsymbol{\alpha}^b$ and $\boldsymbol{\alpha}$), after projection along the direction of $\boldsymbol{n}$ (unit tensor normal to the yield surface). The hardening coefficient h is defined as:

$$h = \frac{b_0}{(\boldsymbol{\alpha} - \boldsymbol{\alpha}_{in}) : \boldsymbol{n}} \exp\left[\mu_0 \left(\frac{p}{patm}\right)^{0.5} \left(\frac{b^M}{b_{ref}}\right)^2\right] \tag{2}$$

with $b^M = (\boldsymbol{r}^M_\alpha - \boldsymbol{\alpha}) : \boldsymbol{n}$ accounting for the distance between memory and yield loci, $\boldsymbol{r}^M_\alpha = \boldsymbol{\alpha}^M + \sqrt{2/3}(m^M - m)\boldsymbol{n}$, and $b_{ref} = (\boldsymbol{\alpha}^b - \tilde{\boldsymbol{\alpha}}^b) : \boldsymbol{n}$ – with all terms defined as shown in Fig. 1. m^M and m are related to the radii of memory and yield surface, respectively, b_0 is a factor depending on the current void ratio and mean effective stress, while μ_0 is a model parameter governing strain accumulation (ratcheting) under drained cyclic loading. At variance with the first SANISAND-MS formulation (Liu *et al.*, 2019b), the yield back-stress ratio $\boldsymbol{\alpha}$ and its projections onto bounding ($\boldsymbol{\alpha}^b$), dilatancy ($\boldsymbol{\alpha}^d$), and critical ($\boldsymbol{\alpha}^c$) surfaces are used here as in SANISAND2004 – see Liu & Pisanò (2019) and Liu (2020).

Experimental observations inspired the evolution laws assumed for the back-stress $\boldsymbol{\alpha}^M$ and size m^M of the memory surface (Liu *et al.*, 2019b). As contractive behaviour promotes 'fabric reinforcement', stages of cyclic contraction are linked to an expansion of the memory surface ($dm^M > 0$), and therefore to larger stiffness through Eqs. (1)–(2). An additional memory-shrinking mechanism ($dm^M < 0$) was also deemed necessary to simulate the loss in stiffness caused by stages of dilative deformation. The proposed incremental law for the memory surface size is expressed as follows:

$$dm^M = \sqrt{\frac{3}{2}} d\boldsymbol{\alpha}^M : \boldsymbol{n} - \frac{m^M}{\zeta} f_{shr} \left\langle -d\varepsilon^p_v \right\rangle \tag{3}$$

where f_{shr} is a geometrical shrinkage factor defined in Liu *et al.* (2019b), while ζ is a material parameter governing the shrinkage rate of the memory surface during dilation. The kinematics of the memory back-stress $\boldsymbol{\alpha}^M$ follows directly from a parallel consistency condition imposed with respect to the memory surface:

$$d\boldsymbol{\alpha}^M = 2/3 \langle \Lambda \rangle h^M (\boldsymbol{\alpha}^b - \boldsymbol{r}^M_\alpha) \tag{4}$$

Compared to SANISAND2004, the formulation of the dilatancy coefficient D was slightly modified by adding a memory-related factor able to enhance sand contractancy after stages of dilative deformation – such a phenomenon is often associated with so-called 'fabric re-orientation'. Further details about constitutive formulation and parameter calibration are available in Liu *et al.* (2019b) and Liu (2020).

All the 3D FE results presented in this paper were obtained using reference SANISAND-MS parameters for the Karlsruhe sand, which is a medium-coarse quartz sand featuring the index properties reported in Table 1 (Wichtmann, 2005). Karlsruhe sand's SANISAND-MS parameters were previously calibrated

Table 1. Karlsruhe sand's index properties – after Wichtmann (2005)

min/max void ratio	min/max dry unit weight	median particle diameter	uniformity coefficient
$e_{min,max}$	$\gamma_{min,max}$	D_{50}	C_u
0.577 – 0.874	13.9 – 16.5 kN/m^3	0.55 mm	1.8

Table 2. Karlsruhe sand's SANISAND-MS model parameters – after Liu *et al.* (2019b).

Elasticity		Critical state					Yield surface	Plastic modulus			Dilatancy		Memory surface		
G_0	ν	M_c	c	λ_c	e_0	ξ	m	h_0	c_h	n^b	A_0	n^d	μ_0	ζ	β
110	0.05	1.27	0.712	0.049	0.845	0.27	0.01	5.95	1.01	2.0	1.06	1.17	260	0.0005	1

by Liu *et al.* (2019b) against the results of single-amplitude high-cyclic traxial tests (10^4 cycles) – see Table 2.

3D FE MODELLING OF MONOPILE-SOIL INTERACTION

Monopile-soil interaction analyses were carried out using the 3D FE modelling capabilities available in OpenSees (sequential version) (McKenna, 2011). Such capabilities were enhanced with an implementation of SANISAND-MS built on the existing SANISAND2004 code from the University of Washington (Ghofrani & Arduino, 2018). This section covers the setup of the reference 3D FE model (see also Corciulo *et al.* (2017) and Taborda *et al.* (2019)), while its accuracy is discussed in the final Appendix.

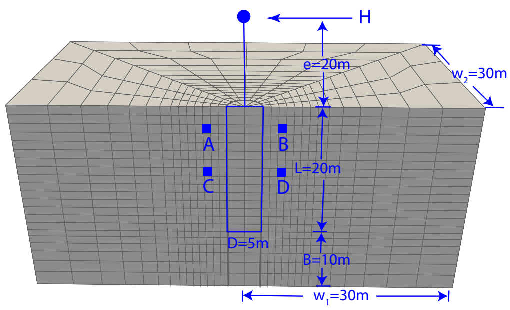

Fig. 2. FE model domain. The reference soil elements (A, B, C, D) are located 2.7 m (A and B) and 9.3 m (C and D) under the ground surface, at a distance of 2.1 m from the monopile shaft.

Soil and monopile

Fig. 2 displays the monopile-soil model adopted in this work, which includes:

- an elastic tubular monopile, with diameter, embedded length and wall thickness representative of typical full-scale monopiles and equal to $D = 5$ m, $L = 20$ m, and $t = 10$ cm, respectively;
- a soil domain with dimensions $[W_1, W_2, L + B] = [30\text{m}, 35\text{m}, 30\text{m}]$ (Fig. 2). Such dimensions are sufficient to avoid domain boundary effects on the lateral response of the pile, as previously shown by Corciulo *et al.* (2017). As the following discussion refers to mono-directional lateral loading, only half domain was modelled for computational convenience;
- lateral loading applied with an eccentricity $e_{ecc} = L =$ 20 m above the soil surface. Such a value is consistent with e_{ecc}/L ratios set in relevant small-scale testing studies (e.g., $e_{ecc} \approx 1.2L$ in LeBlanc *et al.* (2010)), even though (variable) eccentricities in excess of $4L$ may apply to real field conditions (McAdam *et al.*, 2019). The load application point was connected to the 3D pile head at the mudline through an elastic Timoshenko beam.

Boundary conditions were imposed on the soil domain to obtain fully fixed bottom surface, free upper surface, and no horizontal displacement along the direction perpendicular to the lateral surface. Both the soil and the embedded monopile were discretised using 8-node, one-phase SSP brick elements, featuring a stabilised, single-point formulation already proven effective against shear/volumetric locking issues in elasto-plastic media (McGann *et al.*, 2015). Non-linear static simulations of cyclic pile loading were performed using implicit time integration, with iterative solution of each step based on the Krylov–Newton algorithm described by Scott & Fenves (2003). Each (sinusoidal) load cycle was partitioned into 60 step increments, with global convergence tested against a relative error tolerance of 10^{-3} on the displacement solution vector. SANISAND-MS constitutive equations were integrated in time at individual stress points using an explicit, fourth-order Runge-Kutta (RK) algorithm, featuring automatic error control and sub-stepping (Sloan, 1987; Tamagnini *et al.*, 2000; Sloan *et al.*, 2001). RK stress integration requires the input of separate tolerances for plasticity activation and sub-stepping, which were set to $FTOL = 10^{-4}$ kPa (computed value of the yield function) and $STOL = 10^{-4}$ (dimensionless), respectively – see Appendix.

While the SANISAND-MS parameters in Table 2 were adopted for the soil (Wichtmann, 2005; Liu *et al.*, 2019b), typical values of Young's modulus ($E_{steel} = 221$GPa) and Poisson's ratio ($\nu_{steel} = 0.3$) were set for the monopile steel. Following the simplified approach by Griffiths (1985), the pile-sand interface was modelled by introducing around the pile a thin layer of soil bricks with 'degraded' SANISAND-MS properties, so as to heuristically reproduce possible installation effects – though without attempting to model soil-pile gaping during cyclic loading (Day & Potts, 1994; Cerfontaine *et al.*, 2015). The interface layer in the final model was as thick as $\backsim 1\%$ of the monopile diameter; its constitutive parameters were assumed to differ from those in Table 2 only in terms of

Table 3. Numerical simulation programme and corresponding T_b-T_c values inferred from FE results based on Eq. (6) with a single accumulation exponent ($\alpha = 0.5$).

Test label	D_r	ζ_b	ζ_c	T_b	T_c	Test label	D_r	ζ_b	ζ_c	T_b	T_c
L1	30%	0.5	0	0.1	1	D1	70%	0.5	0	0.2	1
L2	30%	0.3	0	0.08	1	D2	70%	0.3	0	0.12	1
L3	30%	0.1	0	0.06	1	D3	70%	0.1	0	0.045	1
L4	30%	0.05	0	0.04	1	D4	70%	0.05	0	0.026	1
L5	30%	0.025	0	0.022	1	D5	70%	0.025	0	0.017	1
L6	30%	0.0125	0	0.014	1	D6	70%	0.0125	0	0.01	1
L7	30%	0.3	0.7	0.08	0.4	D7	70%	0.3	0.7	0.12	0.3
L8	30%	0.3	0.5	0.08	0.6	D8	70%	0.3	0.5	0.12	0.6
L9	30%	0.3	0.3	0.08	0.8	D9	70%	0.3	0.3	0.12	0.8
L10	30%	0.3	-0.25	0.08	1.1	D10	70%	0.3	-0.25	0.12	1.2
L11	30%	0.3	-0.5	0.08	0.8	D11	70%	0.3	-0.5	0.12	0.8
L12	30%	0.3	-0.75	0.08	0.5	D12	70%	0.3	-0.75	0.12	0.6

dimensionless shear modulus ($G_0 = 94$) and critical stress ratio ($M_c = 0.96$).

Prior to the cyclic phase, stresses and internal variables in the FE model were in all cases initialised through standard gravity loading with the pile already 'wished in place' (WIP). In particular, the memory surface was initially set to coincide everywhere with yield surface, i.e., $m^M = m$ (cf. Eq. (3) to Table 2). This is clearly a crude simplification of reality, in that it excludes expected installation effects from the cyclic response of the pile. In this respect, Staubach *et al.* (2020) recently compared the cyclic tilt returned by 'explicit' 3D FE analyses for monopiles either WIP or jacked/impact-driven, with the latter cases studied via Coupled Eulerian-Lagrangian simulations. The authors found WIP-based tilt predictions on the conservative side, although further parametric studies are certainly needed to corroborate such a conclusion. A growing body of experimental research on this subject is currently contributing to filling knowledge gaps related to pile installation effects (Anusic *et al.*, 2019; Heins *et al.*, 2020; Metrikine *et al.*, 2020).

Numerical simulation programme

Although non-stationary and multi-directional in nature (Rudolph *et al.*, 2014; Richards *et al.*, 2019), only unidirectional lateral loading applied in single-amplitude cycles was considered in this first study. The core of this work's FE simulation programme relates to the cases listed in Table 3, with two values of initial sand's relative density, $D_r = 30\%$ and 70%. Such values were selected as representative of generally loose and dense sand, though without trying to match specific soil conditions in the selected reference experiments (see next section). In all cases, the total number of cycles was limited to $N = 100$, which resulted in a calculation time of approximately 49 hours on a computer equipped with an Intel Xeon W-2125 cpu (processor base frequency: 4.0 GHz). The duration of (sequential) 3D FE simulations was mostly affected by the number/density of finite elements in the soil domain (Fig. 2), the degree of soil non-linearity mobilised by the applied loads, and the algorithmic settings in both global (Krylov–Newton) and stress-point (RK) time integration – see Appendix.

The simulation programme in Table 3 was conceived to investigate the influence of different (non-symmetric) cyclic loading conditions on the cyclic tilt of monopiles. In particular, minimum/maximum lateral load values (H in Fig. 2) were selected to modify the amplitude and asymmetry of cyclic loading according to the dimensionless load factors defined by LeBlanc *et al.* (2010):

$$\begin{aligned}\zeta_b &= \frac{H_{max}}{H_{ref}} = \frac{M_{max}}{M_{ref}} \\ \zeta_c &= \frac{H_{min}}{H_{max}} = \frac{M_{min}}{M_{max}}\end{aligned} \tag{5}$$

where H_{max} (M_{max}) and H_{min} (M_{min}) stand for maximum and minimum horizontal load (moment at mudline), respectively. H_{ref} (M_{ref}) is the horizontal force (moment) associated with a 'conventional' definition of lateral capacity, here assumed to correspond with a lateral deflection of $0.1D$ at the ground surface. Accordingly, H_{ref} values equal to 26800 kN and 15450 kN were determined through 3D FE calculations for $D_r = 70\%$ and $D_r = 30\%$, respectively, and the same load eccentricity in Fig. 2. Table 3 includes loading cases associated both with one-way ($\zeta_c \geq 0$, positive H_{max} and H_{min}) and (biased) two-way loading ($-1 \leq \zeta_c < 0$, positive H_{max} and negative H_{min}).

SANISAND-MS 3D FE SIMULATION OF CYCLIC MONOPILE BEHAVIOUR

After some observations on the simulated pile response to monotonic and two-way/symmetric loading, general features of the 3D FE results associated with Table 3 are discussed and broadly compared to selected 1g small-scale test data from the literature, particularly those reported by LeBlanc *et al.* (2010) and Richards *et al.* (2019) – see experimental settings in Table 4. As different soil/pile/loading settings were considered in numerical simulations and reference experiments, the main goal is to verify whether SANISAND-MS can generally reproduce expected features of cyclic sand-monopile interaction. Nonetheless, the important difference related to the total number of loading cycles in the reference experiments (thousands) and 3D FE simulations (one hundred) should also be borne in mind. In what follows, the term 'pile head' is always used for brevity in lieu of 'at the level of soil surface'.

Table 4. Specifications of selected $1g$ small-scale tests.

	Sand properties	Pile test settings
LeBlanc *et al.* (2010)	*Yellow Leighton Buzzard 14/25* $D_{50,10}$=0.81, 56 C_u=1.55 $\gamma_{max,min}$=17.64, 14.43 kN/m^3 ϕ_{cr}=34.3°	L=360 mm D=80 mm t=2 mm e_{ecc}=430 mm
Richards *et al.* (2019)	*Yellow Leighton Buzzard* $D_{50,10}$=0.8, 0.63 mm C_u=1.35 $\gamma_{max,min}$=17.58, 14.65 kN/m^3 ϕ_{cr}=34.3°	L=320 mm D=80 mm t=5 mm e_{ecc}=800 mm

Monotonic behaviour

As a first step, the simulated monotonic behaviour of the monopile was considered. Fig. 3 shows a comparison between the monotonic responses obtained though 3D FE modelling and reported by Achmus *et al.* (2020) after full-scale field tests. The field data from Achmus *et al.* (2020) were considered suitable for such a comparison in that they relate to two monopiles, P3 and P4, of dimensions similar to those in the reference numerical model, i.e., $D = 4.3$ m and $L = 18.5$ m (cf. to $D = 5$ m and $L = 20$ m in Fig. 2). Only for this monotonic loading case, the load eccentricity in the FE model was reduced to 1 m above the ground surface, in order to match the setup in Achmus *et al.*'s tests. The same Karlsruhe sand parameters in Table 2 were retained, as it was not attempted to reproduce in detail the behaviour of the 'medium to very dense sand' at the site. Nevertheless, distinct FE simulations were performed for the cases of dry and fully saturated sand ($D_r = 70\%$), so as to highlight the impact of stress-dependent soil stiffness.

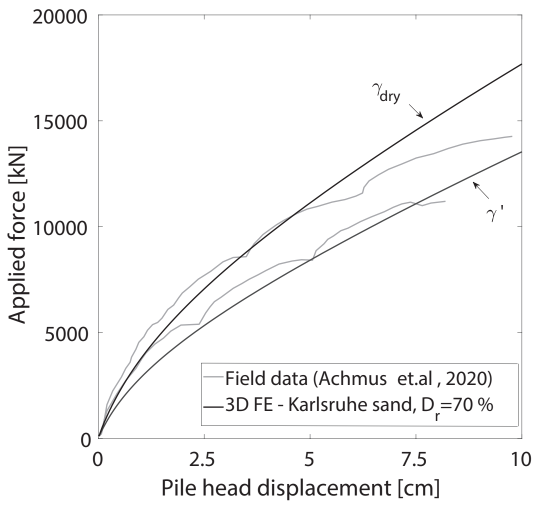

Fig. 3. Comparison between monotonic monopile responses from 3D FE modelling (Karlsruhe sand, $D_r = 70\% - \gamma_{dry} = 15.3$ kN/m^3 and $\gamma' = 9.4$ kN/m^3) and field testing (from Achmus *et al.* (2020), piles P3-P4).

Despite of the differences in pile geometry, installation method (WIP vs impact- and vibro-driven), and soil conditions, the comparison in Fig. 3 confirms that the SANISAND-MS 3D FE model can produce monotonic pile responses in general agreement with reality.

Behaviour under two-way/symmetric cyclic loading

Fig. 4 provides further insight into the SANISAND-MS FE model performance with respect to two-way/symmetric cyclic loading (i.e., with $\zeta_c = -1$). Fig. 4a shows the cyclic response simulated for the reference monopile in dense Karlsruhe sand ($D_r = 70\%$) under 25 loading cycles of different amplitude, i.e., $\zeta_b = 0.1, 0.2, 0.4$. It is readily visible that, prior to reaching a steady state, the pile experiences in all cases some net tilt, alongside a gradual stiffening of the response cycles. A similar response to symmetric cyclic loading has been very recently reported by Richards *et al.* (2021) after centrifuge testing at 80g (i.e., representative of a large-scale monopile). Even in the case of an initially homogeneous system, symmetric loading can gradually induce 'asymmetry' in sand's conditions when applied laterally. Changes in sand fabric (and stiffness) develop in the soil in a way specific to the loading sequence, and therefore not synchronously/symmetrically around the pile. This may be even more true in reality due to inevitable initial inhomogeneities, which may in turn promote some net pile tilt under symmetric loading. The extent of the pile tilt resulting from SANISAND-MS FE simulations is not only a function of the cyclic load amplitude, but also of the fabric-memory effects that are inherent to the constitutive model. In the last respect, Fig. 4a also shows the FE response obtained for $\zeta_b = 0.2$ after inhibiting the memory surface mechanism in SANISAND-MS (i.e., after setting $\mu_0 = \beta = 0$ in Table 2). It is readily apparent that, in the absence of sand stiffening during cycling, the cyclic response (i) reaches more quickly a steady state, and (ii) exhibits only very limited net tilt under symmetric loading. This occurrence underlines the importance of 'realistically' initialising the memory surface locus (i.e., m^M and $\boldsymbol{\alpha}^M$ in Eqs. (3)-(4)), for instance with respect to specific effects of pile installation. It is anticipated that preliminary simulation of the pile driving process could return distributions of m^M and $\boldsymbol{\alpha}^M$ that would potentially result in (more) realistic evolution of monopile stiffness and tilt under cyclic loading.

It seems interesting to discuss whether the FE response to symmetric loading complies, at the macroscale, with a typical Masing-type representation. In Fig. 4b the steady cycles (black solid lines, re-centred with respect to the (0;0)) from Fig. 4a for different ζ_b values are plotted together with their closest 'Masing fitting' (black dashed lines). Even though bounding surface models do not produce stress-strain response cycles exactly compliant with Masing's idealisation (Borja & Amies, 1994), the simulated pile behaviour appears to match a Masing-type response at the global scale, which is in agreement with the experimental findings of Abadie *et al.* (2019a). However, Fig. 4b also shows that the reference Masing cycles (black dashed lines) could not be built on the initial/monotonic 3D FE response branch (green line), but rather on stiffer branches (magenta lines) that represent the lateral pile stiffness in the last cycle applied with a specific load amplitude. This fact is a consequence of the cyclic soil stiffening simulated

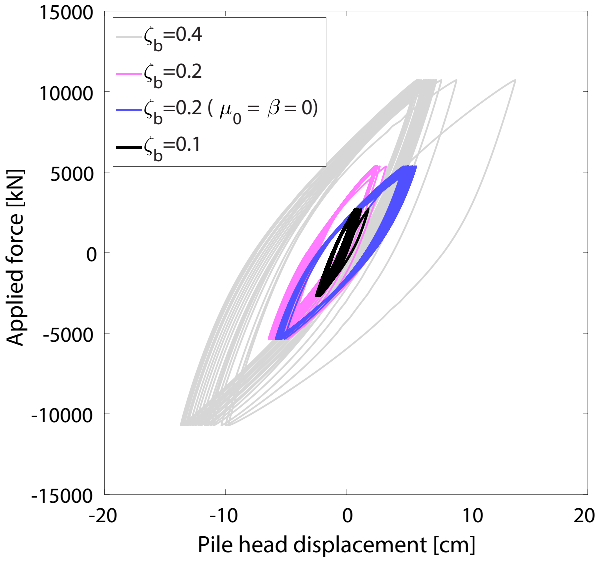

(a) induced asymmetry in the tilting response

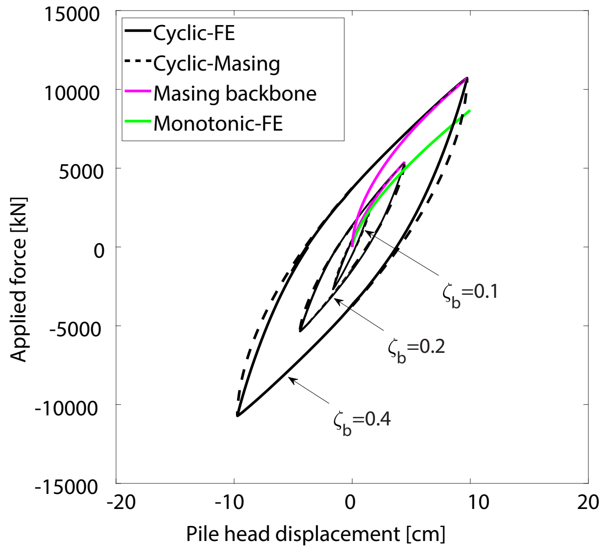

(b) compliance with the Masing rule

Fig. 4. Simulated monopile response to symmetric cyclic loading of different amplitude ($\zeta_b = 0.1, 0.2, 0.4$ and $D_r = 70\%$).

by SANISAND-MS through its memory surface hardening mechanism (cf. to Fig. 4a).

Behaviour under one-way cyclic loading

This subsection describes in more detail general response features under one-way cyclic loading (i.e., with $\zeta_c \geq 0$), which is most relevant to monopile tilting (Klinkvort, 2013). Typical cyclic responses recorded at the pile head are plotted in Fig. 5 for the simulation cases D2 and L2 in Table 3. Figs. 5a and 5b clearly show that the pile head displacement induced by the first monotonic loading (i.e., up to point P in the figures) is (i) weakly affected by D_r (this is consistent with applying a maximum loads of equal relative magnitude ζ_b), and (ii) is significantly larger than the displacement produced within each of the subsequent loading cycles. Displacement accumulation can be observed to progress under cyclic loading at a gradually decreasing rate. This kind of global ratcheting behavior appears to be fully related to the local ratcheting exhibited by sand samples during cyclic laboratory tests (Wichtmann, 2005; Liu *et al.*, 2019b).

Complementary visualisation of the pile tilting response is provided in Fig. 5c in terms of accumulated displacement/rotation against the number of cycles N. For given load settings, the relative density has clearly a quantitative impact on the accumulation of permanent pile rotation, as indicated by available experimental data (LeBlanc *et al.*, 2010).

In this respect, it is common to plot rotation accumulation trends after normalisation with respect to a reference rotation θ_s defined by LeBlanc *et al.* (2010) as the rotation that would occur in a static test when the load is equivalent to the maximum cyclic load. Numerical results regarding monopile tilt accumulation are displayed in the following in the normalised $\Delta\theta/\theta_s$ form, where $\Delta\theta = \theta_N - \theta_0$ is the difference between the rotation accumulated after N cycles (θ_N) and the

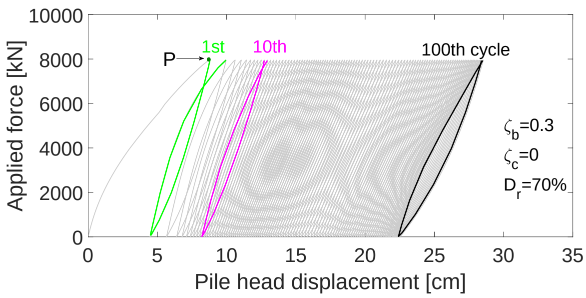

(a) Lateral force vs pile head displacement ($D_r = 70\%$)

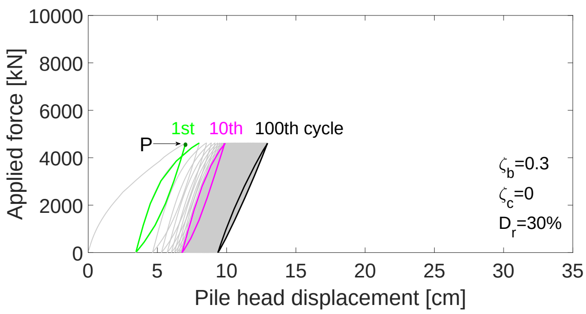

(b) Lateral force vs pile head displacement ($D_r = 30\%$)

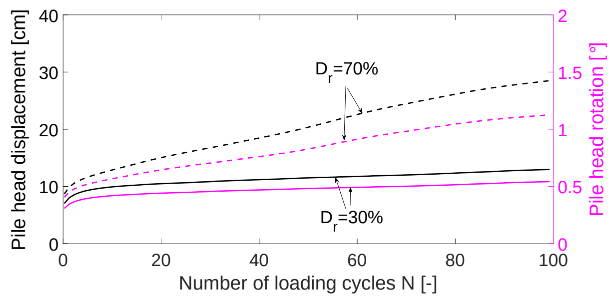

(c) Pile head displacement/rotation vs number of cycles

Fig. 5. Cyclic pile head response resulting from SANISAND-MS 3D FE simulations – simulation cases D2 and L2 in Table 3.

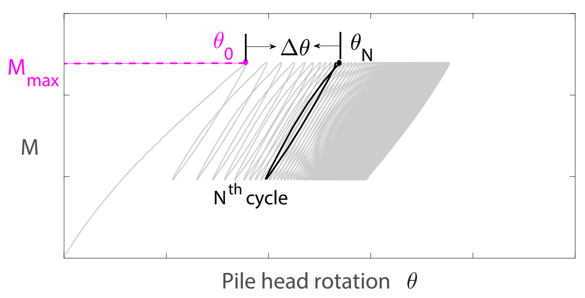

Fig. 6. Definition of reference pile rotation values.

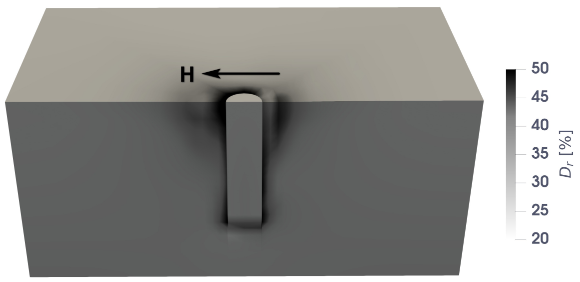

(a) Initial $D_r = 30\%$**, 100th cycle**

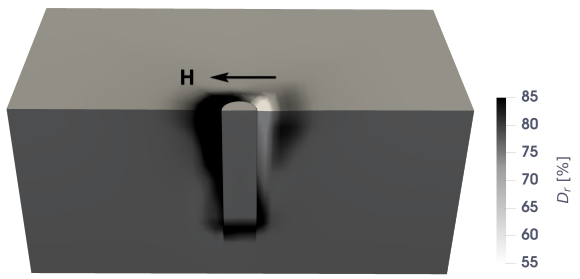

(b) Initial $D_r = 70\%$**, 100th cycle**

Fig. 7. Distribution of sand relative density (D_r) **after 100 loading cycles – simulations cases L2 (a) and D2 (b) in Table 3.**

rotation at the end of the pre-cycling monotonic phase (θ_0) (see Fig. 6). Although θ_s and θ_0 may not exactly coincide when obtained experimentally, it is accurate to assume $\theta_s = \theta_0$ within the adopted modelling framework.

Each of the performed 3D FE analyses returned detailed 'numerical data' about the cyclic response of sand during pile loading, including the evolution of stresses, strains, and all internal/hardening variables in the SANISAND-MS formulation. For example, interesting indications are provided by the pseudo-colour plots in Fig. 7, in which the relative density distribution at the end of the 100th cycle is displayed for the same cases $L2$ ($D_r = 30\%$) and $D2$ ($D_r = 70\%$). The D_r plots in Fig. 7 confirm well-established evidence about cyclic sand densification (Cuéllar *et al.*, 2009), e.g., regarding D_r variations being relatively more pronounced in loose sand. As the selected FE results refer to pure one-way loading ($\zeta_b = 0.3, \zeta_c = 0$), asymmetric sand densification is predicted on the opposite sides of the pile. In the case of dense sand, some net sand loosening is also visible along the upper shaft (on the back-side with respect to the loading direction), due to compression relief and shear-induced dilation.

The final D_r distributions in Fig. 7 are an outcome of the local response history at soil element. Relevant features of such a response are illustrated in Figs. 8-11, particularly for the reference elements (A, B, C, D) indicated in Fig. 2 and the simulations cases $L2$ ($D_r = 30\%$) and $D2$ ($D_r = 70\%$). Fig. 8 shows cyclic strain paths in terms of deviatoric and volumetric strain invariants, with the colour sidebars indicating the number of cycles gradually elapsed. The intensity of soil straining depends on the specific location of each reference element, and it was expected that shallow elements on the front-side of the pile (i.e., within the 'passive' soil mass) would experience overall larger deformation with a more pronounced volumetric component – note that the strain paths at elements A-B (Figs. 8a-8b) are steeper than at elements C-D (Figs. 8c-8d). The timing of soil straining along the cyclic history appears to depend both on the soil location and the initial relative density. For instance, the dependence on D_r is particularly evident for elements A and C (Fig. 8a): in the case of $D_r = 30\%$, the soil deforms mostly during the first 30 cycles, so that the response to the remaining 70 cycles develops at nearly constant volume. The ratcheting response of the soil is directly related in SANISAND-MS to the evolution of the memory locus, particularly of its size m^M (Fig. 1). Fig. 9 confirms the close correlation between the strain paths in Fig. 8 and the evolution of m^M against the number of cycles. The rate of m^M variations reflects how quickly the soil approaches a state of larger stiffness and slower strain accumulation, which is phenomenologically represented by an expanded memory surface (Liu *et al.*, 2019b). 'Irregular' $m^M - N$ trends such as those simulated for element A are indicative of alternating expansion and contraction of the memory surface, with the latter being triggered by volumetric dilation according to Eq. (3). Generally, the memory surface is more likely to exhibit such a behaviour at shallow soil locations, i.e., where the mean effective stress is low and dilation more easily triggered.

The stress paths simulated at the same reference points are displayed in Fig. 10 in terms of mean effective stress (p) and deviatoric stress invariant (q) – for brevity, only for the case of $D_r = 70\%$. As observed for their strain counterparts, also stress paths evolve during cycling at a rate depending on several governing factors. It seems interesting to observe that, while strain paths may cyclically evolve towards (nearly) isochoric conditions (Fig. 8), a gradual decrease in p takes place, up to the attainment of 'undrained-like' $q - p$ response loops – see, e.g., elements B-C. Fig. 11 reveals the extent of such a phenomenon by showing the distribution of the p/p_{in} ratio between the final ($N = 100$, at minimum/nil lateral load) and the initial (after gravity loading) values of mean effective stress. Both in loose and dense sand, an extended mass of soil around the pile reaches p/p_{in} values lower than 1, particularly where severe shear loading occurs. Repeated shear loading causes a gradual densification of the soil, which is accompanied by

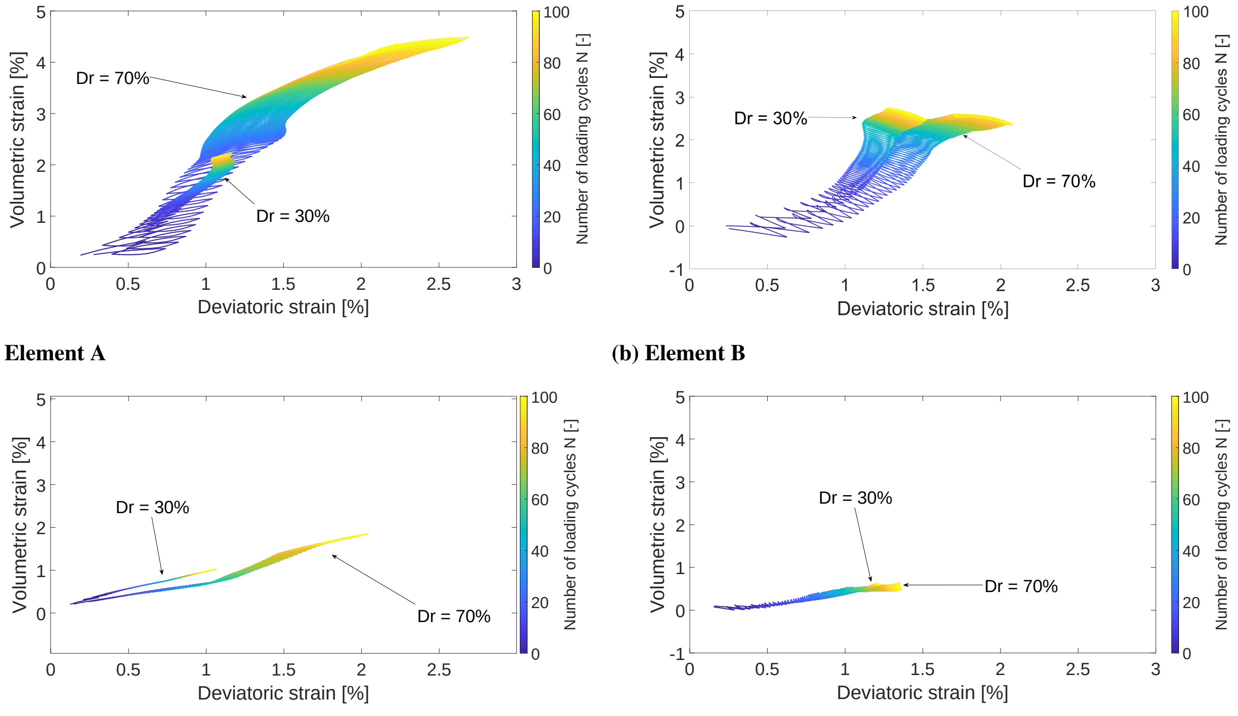

(a) **Element A** (b) **Element B**

(c) **Element C** (d) **Element D**

Fig. 8. Cyclic strain paths at the reference elements in Fig. 2. Values of volumetric and deviatoric strain invariants were obtained from the total (ε_{ij}) and deviatoric (e_{ij}) strain tensors as ε_{kk} and $\sqrt{(2/3)e_{ij}e_{ij}}$, respectively. Simulation cases L2 and D2.

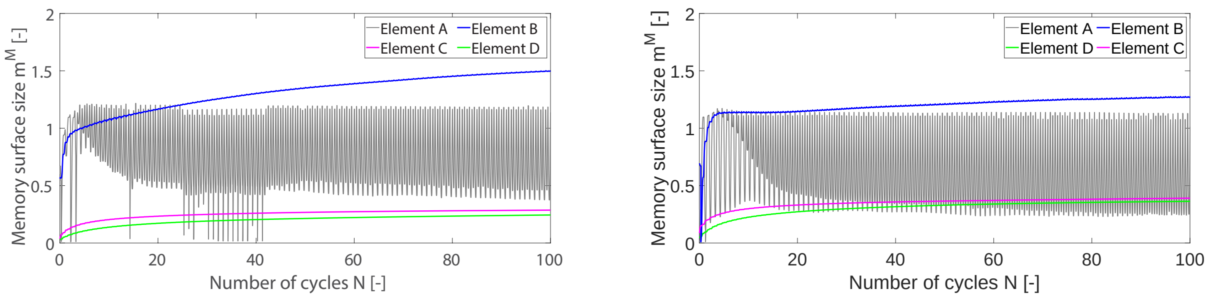

(a) $D_r = 30\%$ **(b)** $D_r = 70\%$

Fig. 9. Evolution of the memory surface size at the reference elements in Fig. 2 – simulation cases (a) L2 and (b) D2.

the observed reduction in mean stress due to the continuity of contiguous soil elements around the pile. The same kind of interaction between cyclic loading and kinematic constraints, as well as similar undrained-like stress paths, have been recorded experimentally by Tsuha *et al.* (2012) during small-scale tests on piles subjected to axial cyclic loading. The final achievement of a certain p/p_{in} distribution are clearly a function of the specific soil behaviour, as well as of the magnitude, asymmetry, and duration of the enforced cyclic loading.

Although more complex than in element test analyses, the simulated soil response around a monopile complies well with the intended performance of the SANISAND-MS model (Liu *et al.*, 2019b, 2020). Nonetheless, a note should be made about the calibration of sand's parameters in relation to monopile applications. While 3D FE results suggest that significant strain accumulation occurs at shallow soil locations, the reference SANISAND-MS parameters in Table 2 were identified against high-cyclic triaxial test results obtained under relatively large mean effective stress – equal to 100-200 kPa in most cases. This aspect should be carefully considered in the planning of future high-cyclic testing programmes, so as to enable more accurate modelling of cyclic behaviour at low confinement.

COMPARISON TO MONOPILE TILT DATA

In this section the tilting of the monopile returned by SANISAND-MS 3D FE analyses is discussed in more detail in comparison to existing experimental evidence. Given the limited number of simulated cycles ($N = 100$), however, the numerical results in hand do not directly relate to the long-term loading experienced by real monopiles in the field. Nonetheless, such a limitation should not devalue a modelling framework that supports in-depth

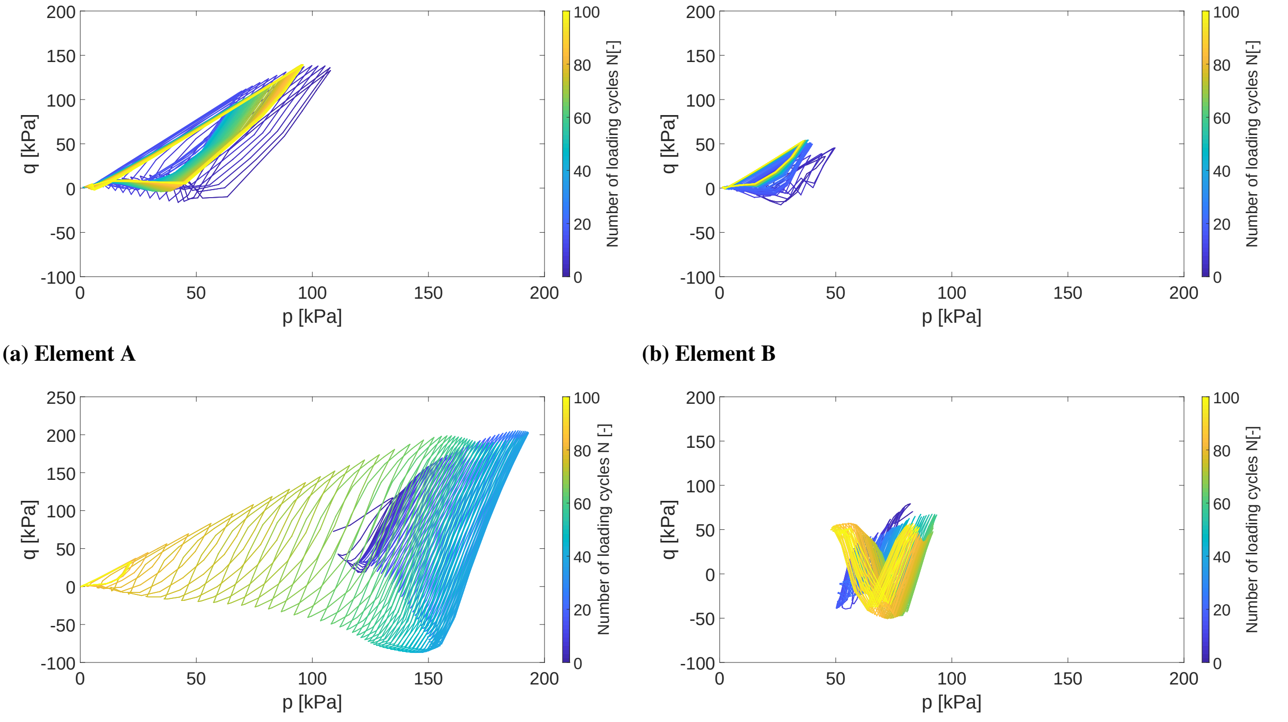

(a) Element A **(b) Element B**

(c) Element C **(d) Element D**

Fig. 10. Cyclic effective stress paths at the reference elements in Fig. 2. Values of mean and deviatoric stress invariants were obtained from the effective stress tensor (σ_{ij}) and deviatoric (s_{ij}) effective stress tensors as $\sigma_{kk}/3$ and $\sqrt{(3/2)s_{ij}s_{ij}} \cdot \cos(3\theta_\sigma)$, respectively, where θ_σ stands for the Lode angle. Simulation case D2.

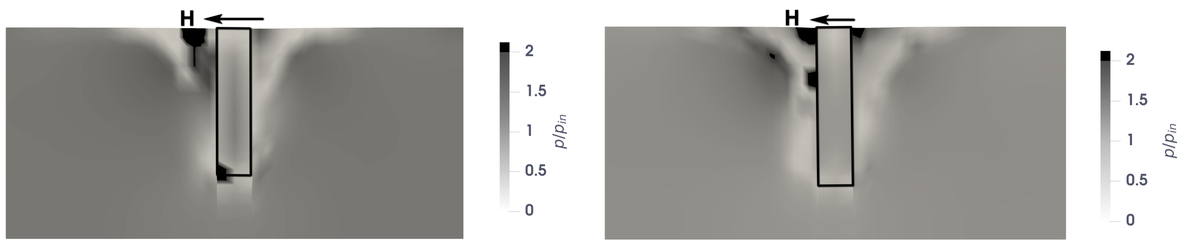

(a) Longitudinal/vertical section, initial $D_r = 30\%$ **(b) Longitudinal/vertical section, initial $D_r = 70\%$**

Fig. 11. Distribution of the p/p_{in} ratio between the final ($N = 100$, nil lateral load) and the initial (after gravity loading) values of mean effective stress – simulation cases (a) L2 and (b) D2.

understanding of geotechnical mechanisms (see previous section) and, potentially, a mechanics-based refinement of design approaches.

Experimental and numerical results regarding monopile tilt are compared in Fig. 12 in relation to pure one-way cyclic loading ($\zeta_c = 0$) of different amplitude ratio ζ_b (Eq. (5)) – 3D FE tilt trends were plotted by selecting, for each cycle, monopile rotation values associated with the maximum load amplitude. $1g$ small-scale experimental results from Richards *et al.* (2019) (Fig. 12a – $D_r = 1\%$, and Fig. 12b – $D_r = 60\%$) and LeBlanc *et al.* (2010) (Fig. 12c – $D_r = 4\%$, and Fig. 12d – $D_r = 38\%$) were selected for semi-quantitative comparison. A well-known point of attention about 1g physical modelling regards the scaling of sand's dilatancy, which is inherently stress-dependent (Bolton, 1986): the behaviour of a prototype pile in medium-dense/dense sand is best reproduced in 1g scaled tests using a lower relative density, given the larger dilatancy that sand exhibits at low stress levels. The interested reader is referred to LeBlanc *et al.* (2010) and Richards *et al.* (2019) for further discussion of geotechnical scaling in pile-sand models. The tests selected from LeBlanc *et al.*'s and Richards *et al.*'s database were deemed representative of soil conditions broadly comparable to those assumed in the (full-scale) FE model – i.e., to a monopile in loose and dense sand. Out of the simulation programme in Table 3, the 3D FE results obtained for the cases L1–L3 and D1–D3 are illustrated in Figs. 12e ($D_r = 30\%$) and 12f ($D_r = 70\%$).

Both experimental and simulation results indicate that, under pure one-way cyclic loading, higher ζ_b values lead to the accumulation of larger pile rotation. Quantitatively, 3D FE simulations returned $\Delta\theta/\theta_s$ values in the order of 10^0 after 100 cycles. Such values are consistent with the experimental data reported by LeBlanc *et al.* (2010), who obtained normalised rotation values of about $7 \sim 8 \times 10^{-1}$ under similar cyclic

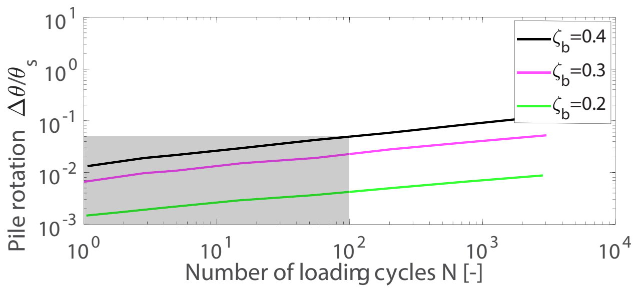

(a) $D_r = 1\%$**, experimental data from Richards *et al.* (2019)**

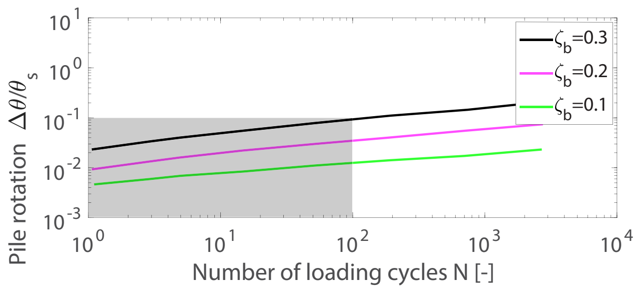

(b) $D_r = 60\%$**, experimental data from Richards *et al.* (2019)**

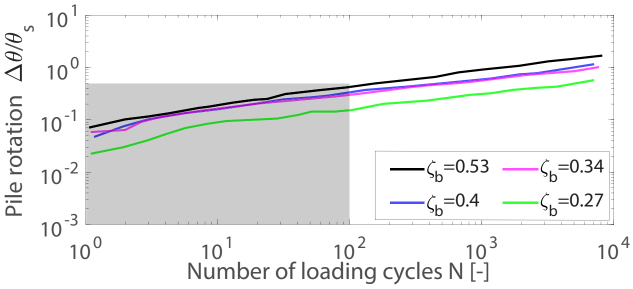

(c) $D_r = 4\%$**, experimental data from LeBlanc *et al.* (2010)**

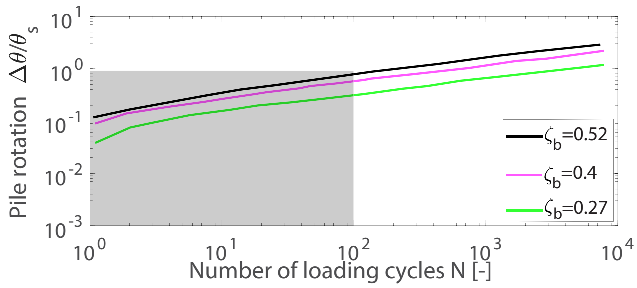

(d) $D_r = 38\%$**, experimental data from LeBlanc *et al.* (2010)**

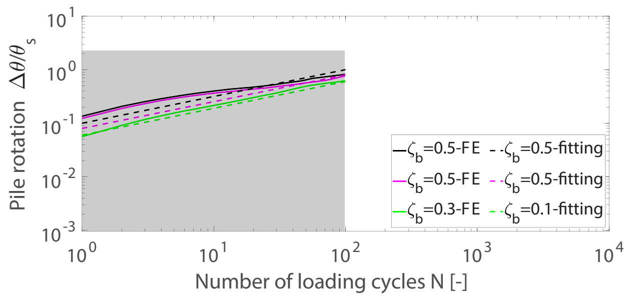

(e) $D_r = 30\%$**, SANISAND-MS 3D FE results**

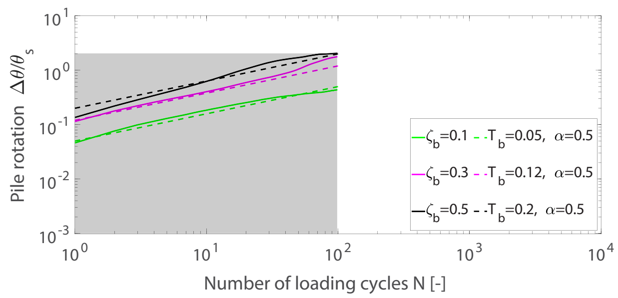

(f) $D_r = 70\%$**, SANISAND-MS 3D FE results**

Fig. 12. Influence of the cyclic load amplitude ratio (ζ_b) on the normalised pile rotation ($\Delta\theta/\theta_s$) against the number of loading cycles (N). Both Experimental and 3D FE results correspond with pure one-way cyclic loading ($\zeta_c = 0$).

loading conditions. In contrast, Richards *et al.*'s data show after 100 cycles smaller $\Delta\theta/\theta_s - N$ values. In this respect, it should also be recalled that SANISAND-MS parameters were originally calibrated to achieve best agreement with soil test data over 10^4 cycles (Wichtmann, 2005; Liu *et al.*, 2019b). In fact, quantitatively different FE results could be obtained after alternative calibration choices.

Fig. 13 displays the influence of a positive asymmetry ratio ζ_c on monopile tilting under biased one-way cyclic loading (i.e., with no change in the sign of the load), for the case of $\zeta_b = 0.3$. SANISAND-MS 3D FE results (Fig. 13c – $D_r = 30\%$, and Fig. 13d – and 70%; simulations L7, L8, L9 and D7, D8, D9 in Table 3) and experimental data from LeBlanc *et al.* (2010) (Fig. 13a – $D_r = 4\%$, and Fig. 13b – $D_r = 38\%$) are compared in the figure, and support altogether the following conclusions:

1. nearly linear tilt accumulation trends in bi-logarithmic plots;
2. the accumulated rotation after 100 cycles lies in the $10^{-1} - 10^{0}$ range;
3. a lower accumulated rotation is obtained at increasing ζ_c when $\zeta_c \geq 0$.

3D FE and experimental results could be further compared as in Figs. 12-13 for cases of two-way cyclic loading (i.e., with negative ζ_c – simulations cases L10, L11, L12 and D10, D11, D12 in Table 3). However, it was preferred to prioritise in the following a broader assessment of 3D FE results against existing simplified approaches for monopile tilt calculations. In particular, recent experimental studies have supported the use of the following empirical relationship (LeBlanc *et al.*, 2010):

$$\frac{\Delta\theta}{\theta_s} = T_b\left(\zeta_b\right) T_c\left(\zeta_c\right) N^{\alpha} \tag{6}$$

which enables straightforward quantification of the normalised monopile rotation under single-amplitude, unidirectional cyclic loading. In Eq. (6) T_b and T_c are dimensionless functions separately accounting for the influence of ζ_b and ζ_c, respectively, while α is a ratcheting exponent; in particular, the definition of T_c is such that $T_c(\zeta_c = 0) = 1$ and $T_c(\zeta_c = 1) = 0$. LeBlanc *et al.* (2010) recognised that T_b increases linearly with ζ_b depending on the relative density, whereas T_c was found to be a D_r-insensitive, non-monotonic function of ζ_c; the same authors proposed for their dataset a single value of the ratcheting exponent, $\alpha = 0.31$, unaffected by D_r, ζ_b,

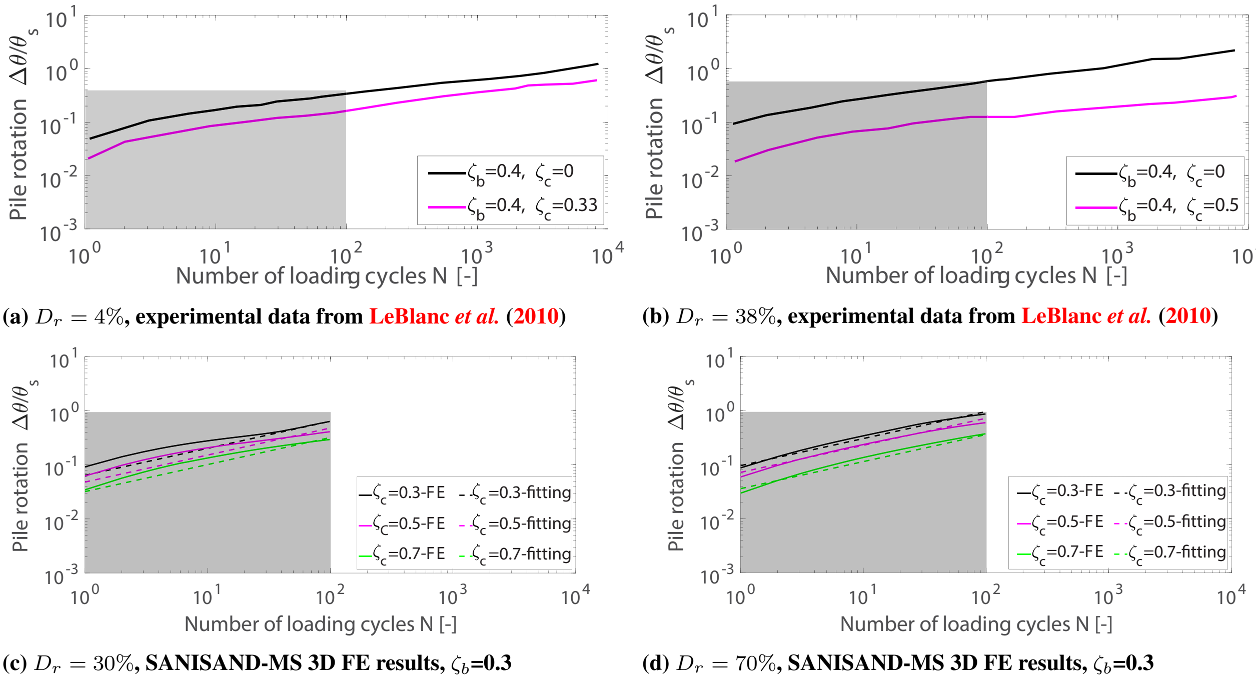

(a) $D_r = 4\%$**, experimental data from LeBlanc *et al.* (2010)**

(b) $D_r = 38\%$**, experimental data from LeBlanc *et al.* (2010)**

(c) $D_r = 30\%$**, SANISAND-MS 3D FE results,** ζ_b**=0.3**

(d) $D_r = 70\%$**, SANISAND-MS 3D FE results,** ζ_b**=0.3**

Fig. 13. Influence of a positive cyclic load asymmetry ratio (ζ_c**) on the normalised pile rotation (**$\Delta\theta/\theta_s$**) against the number of loading cycles (**N**).**

and ζ_c – which differs, however, from the conclusions that Truong *et al.* (2019) drew based on centrifuge test results. As reported in Table 3, T_b-T_c values were also estimated in this study for all FE simulation cases via 'visual' curve fitting of numerical rotation trends. For simplicity, a single value of the ratcheting exponent equal to $\alpha = 0.5$ was identified, although more accurate fitting could be obtained through ζ_c-dependent α values (Truong *et al.*, 2019; Richards *et al.*, 2019).

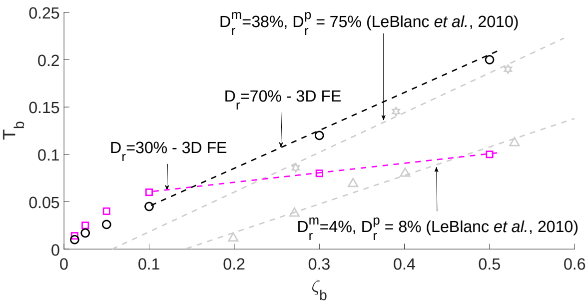

Fig. 14. Comparison between experimental (1g) and numerical $T_b - \zeta_b$ **trends for loose and dense sand – pure one one-way cyclic loading (**$\zeta_c = 0$**). Relative density values for the reference test data are provided for model (**D_r^m**) and prototype (**D_r^p**) scales as per LeBlanc *et al.* (2010).**

The $T_b - \zeta_b$ trends inferred from SANISAND-MS 3D FE results are reported in Fig. 14 alongside those from LeBlanc *et al.* (2010). The reference experimental data suggest that the slope of the $T_b - \zeta_b$ trends increases with the relative density of the sand. The numerical results in Fig. 14 support similar conclusions for ζ_b values larger than 0.1, whereas they deviate from linearity at low amplitude ratios – most apparently for the case of loose sand. Such a non-linearity is compatible with the intuitive fact that no monopile tilt should occur under vanishing cyclic load amplitude. However, existing experimental data do not inform sufficiently about monopile tilt at $\zeta_b < 0.1$, so that more extensive studies, both experimental and numerical, will be necessary to clarify this aspect.

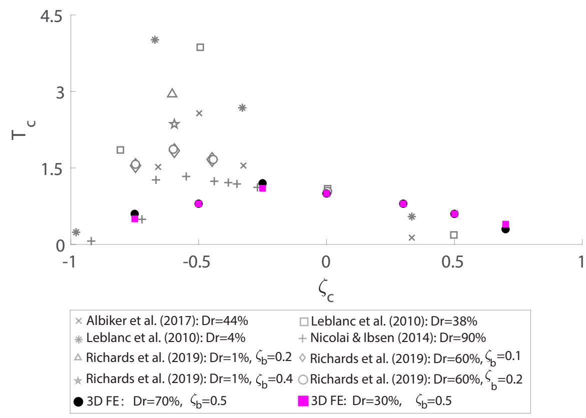

Fig. 15. Comparison between experimental (1g) and numerical $T_c - \zeta_c$ **trends for loose and dense sand.**

Similarly, Fig. 15 presents a comparison between numerical $T_c - \zeta_c$ trends and those associated with selected experimental datasets – namely, from LeBlanc *et al.* (2010); Nicolai & Ibsen (2014); Albiker *et al.* (2017); Richards *et al.* (2019). In agreement with LeBlanc *et al.* (2010)'s observations, the T_c values emerging from numerical simulations are markedly insensitive to D_r. While the simulated $T_c - \zeta_c$ trend agrees qualitatively with all reference data, some quantitative differences are apparent, for instance in terms of maximum T_c and associated value of ζ_c. Such differences may be attributed to different experimental settings, sand characteristics and scaling effects, and will require further studies to be deciphered. For instance, the quantitative impact of different gravity levels in small-scale testing has been recently pointed out by Richards (2019). Overall, Figs. 14-15 confirm that the proposed SANISAND-MS 3D FE framework can produce results in general agreement with experimental evidence, at least within the limited number of loading cycles considered in this study. As shown throughout this work, implicit 3D FE modelling has potential to enhance the detailed interpretation of monopile-soil interaction mechanisms, and enable parametric studies more extensive than feasible through testing.

CONCLUDING REMARKS

In this study, implicit 3D FE modelling was combined with the memory-enhanced, bounding surface SANISAND-MS model to numerically analyse monopile behaviour under lateral cyclic loading in dry sand. The selection of SANISAND-MS was motivated by its proven ability to reproduce cyclic ratcheting in sand samples. Parametric studies were carried out to numerically investigate the link between local soil behaviour and global monopile response to cyclic loading – particularly its lateral tilt. The significant computational costs of implicit 3D FE modelling imposed to limit the numerical study to relatively short loading histories (100 cycles), with obvious impact on the possibility to extend numerical observations to real field conditions.

Semi-quantitative comparison to experimental data from the literature supported the suitability of the proposed modelling approach. In particular, it was possible to confirm typical assumptions usually associated with empirical tilt prediction methods, mostly regarding the relationship between tilting trends and magnitude/asymmetry of (single-amplitude) cyclic loading.

Even when limited to short-term cyclic loading, implicit 3D FE modelling can shed light on the geotechnical mechanisms underlying relevant response features at the foundation level. Importantly, detailed 3D modelling of monopile-soil interaction can help to evaluate the implications of different design choices and/or soil parameters uncertainly estimated. Such possibilities may positively impact the soundness of offshore geotechnical practice, and are not equally enabled by simpler 0D/1D modelling approaches.

Future work along this research line will continue to explore the role of relevant governing factors, such as, e.g., pile slenderness, eccentricity and orientation of the lateral load, pore pressure effects in water-saturated soil. The results presented in this paper encourage more intensive use of implicit SANISAND-MS 3D FE modelling, particularly to inspire enhanced design methods for cyclically loaded foundations – not limited to offshore monopiles.

APPENDIX – ACCURACY OF 3D FE RESULTS

Mesh sensitivity

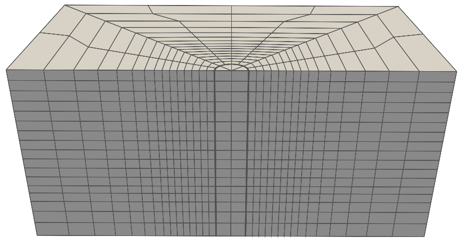

(a) 2399 elements

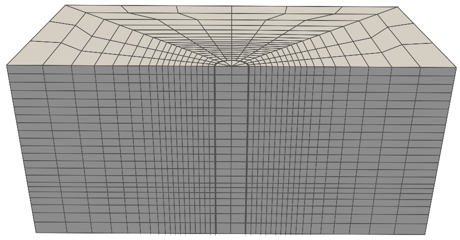

(b) 5571 elements

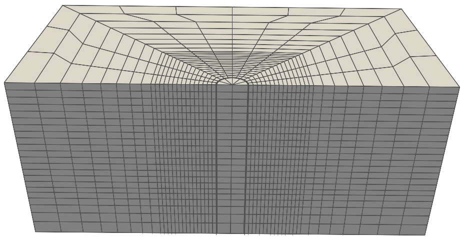

(c) 6755 elements

Fig. 16. Auxiliary 3D FE models adopted for the mesh sensitivity study.

The size of the soil domain in Fig. 2 was determined to prevent boundary effects, in agreement with previous indications from Corciulo *et al.* (2017). Afterwards, the sensitivity of FE results to space discretization was investigated. To this end, the FE results obtained using the four meshes in Fig. 2 and Fig. 16 were compared for the simulation case L6 in Table 3 – total number of SSP elements equal to 2399, 4181, 5571, 6755 in Figs. 16a, 2, 16b, 16c, respectively. Fig. 17 displays the pile responses associated with the four meshes, in terms of force-displacement cycles (Fig. 17a) and accumulated pile displacement against the number of cycles (Fig. 17b). Finer meshes appear to result in larger accumulated displacement. As a converging trend was clearly observed upon mesh refinement, the mesh in Fig. 2 (4181 elements) was finally selected as a trade-off between accuracy and efficiency. It is worth mentioning that the calculation time for (sequential) 3D FE simulations ranged, for 100 loading cycles, from 16 hours (coarsest mesh) to 82 hours hours (finest mesh), and was about 49 hours for the selected mesh in Fig. 2.

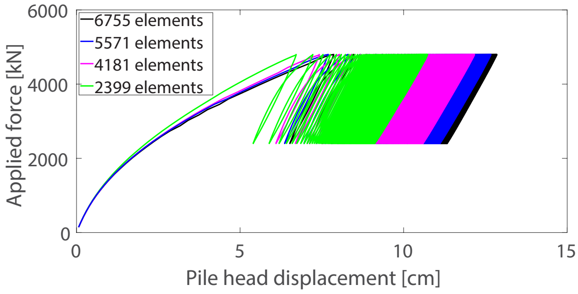

(a) Lateral force vs pile head displacement at soil surface

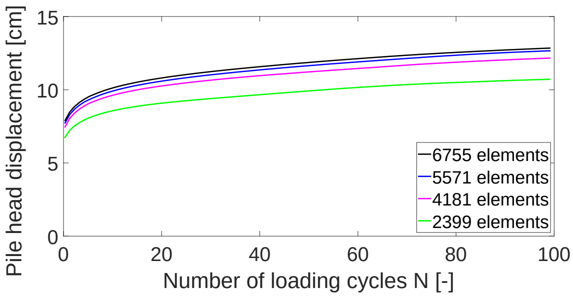

(b) Pile head displacement vs number of loading cycles

Fig. 17. Mesh sensitivity effects in the monopile response to lateral cyclic loading ($D_r = 30\%$, simulation case L6 in Table 3).

Influence of stress-point integration settings

Stress integration at individual Gauss points (one per SSP element) was performed using an explicit Runge-Kutta (RK) algorithm of the type described in Sloan *et al.* (2001). In the authors' experience, explicit integration is well suited for cyclic/dynamic loading conditions, i.e., in the presence of frequent stress reversals. From an implementation standpoint, the adopted RK algorithm:

- features fourth-order accuracy, as in the version described by Sloan (1987);
- operates automatic sub-stepping based on an estimate of the integration error obtained by comparing fourth- and fifth-order RK solutions. Sub-stepping is performed until the estimated (normalised) error is found to be better than an input tolerance $STOL$;
- recognises the local transition from elastic to elasto-plastic response when the computed yield function is larger than $FTOL$.

All the numerical results presented in this work were obtained after setting $STOL = 10^{-4}$ and $FTOL = 10^{-4}$ kPa. Obviously, lower values of $STOL$ and $FTOL$ would be in favour of higher accuracy, though with increased computational burden. Stress integration with error-driven sub-stepping was deemed particularly appropriate for the application in hand, as unreliable FE results would be obtained if numerical errors were left free to accumulate. In contrast, the inclusion of automatic sub-stepping allowed a desired level of accuracy to be preserved across the soil domain, also at shallow soil locations where accurate stress integration is notoriously more difficult.

Figs. 18-19 illustrate the impact of RK integration settings on the stress response simulated at elements B (shallow) and D (deeper) in Fig. 2. In particular, the mean effective stress (p) and the deviatoric stress invariant (q) are plotted against the number of calculation steps for the simulation case L2 in Table 3. To analyse the effects of different RK integration settings, cyclic strain histories were extracted from the reference FE solution at the selected elements, and then re-applied in the RK integration routine to re-calculate stresses for different values of $STOL$ (Fig. 18) and $FTOL$ (Fig. 19). While it is acknowledged that the extracted strain histories would also be affected by the mentioned integration settings, the adopted approach was considered a simpler, yet informative, way to perform the intended analysis. Overall, Figs. 18-19 support the validity of the selected integration settings, as they show that 'harsher' choices would have not produced appreciably different results – not even at shallow soil locations.

ACKNOWLEDGEMENTS

The authors wish to acknowledge the China Scholarship Council (CSC) and the Geo-Engineering Section of Delft University of Technology for financial support of the first author. The detailed and constructive feedback of two anonymous reviewers is also greatly appreciated.

REFERENCES

Abadie, C. N., Byrne, B. W. & Houlsby, G. T. (2019a). Rigid pile response to cyclic lateral loading: laboratory tests. *Géotechnique* **69**, No. 10, 863–876.

Abadie, C. N., Houlsby, G. & Byrne, B. (2019b). A method for calibration of the hyperplastic accelerated ratcheting model (HARM). *Computers and Geotechnics* **112**, 370–385.

Achmus, M., Kuo, Y.-S. & Abdel-Rahman, K. (2009). Behavior of monopile foundations under cyclic lateral load. *Computers and Geotechnics* **36**, No. 5, 725–735.

Achmus, M., Schmoor, K. A., Herwig, V. & Matlock, B. (2020). Lateral bearing behaviour of vibro-and impact-driven large-diameter piles in dense sand. *geotechnik* **43**, No. 3, 147–159.

Albiker, J., Achmus, M., Frick, D. & Flindt, F. (2017). 1 g model tests on the displacement accumulation of large-diameter piles under cyclic lateral loading. *Geotechnical Testing Journal* **40**, No. 2, 173–184.

Anusic, I., Lehane, B., Eiksund, G. & Liingaard, M. (2019). Influence of installation method on static lateral response of displacement piles in sand. *Géotechnique Letters* **9**, No. 3, 193–197.

Arany, L., Bhattacharya, S., Macdonald, J. H., Hogan, S. J. *et al.* (2015). A critical review of serviceability limit state requirements for monopile foundations of offshore wind turbines. In *Offshore Technology Conference*, Offshore Technology Conference.

Archer, C., Simão, H., Kempton, W., Powell, W. & Dvorak, M. (2017). The challenge of integrating offshore wind power in the US electric grid. part I: Wind forecast error. *Renewable energy* **103**, 346–360.

Barari, A., Bagheri, M., Rouainia, M. & Ibsen, L. B. (2017). Deformation mechanisms for offshore monopile foundations

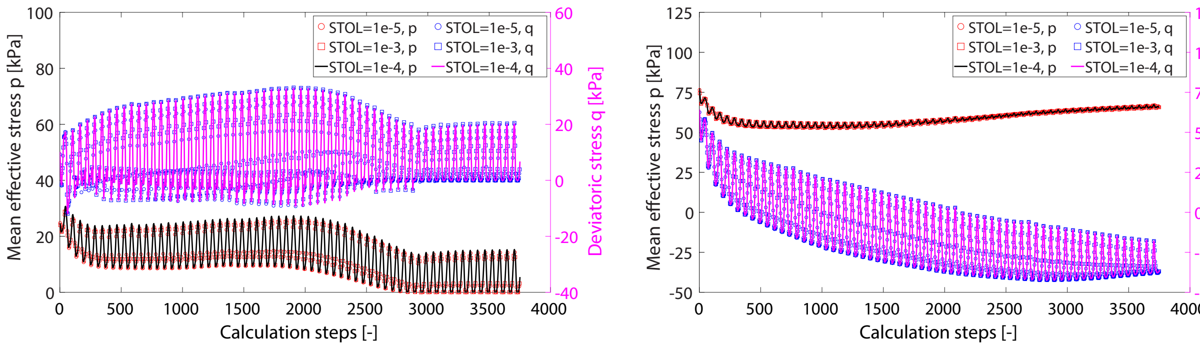

(a) Element B **(b) Element D**

Fig. 18. Influence of $STOL$ (tolerance for error-driven sub-stepping) on stress integration at elements B and D in Fig. 2 – simulation case L2 in Table 3. Values of mean and deviatoric stress invariants were obtained from the total (σ_{ij}) and deviatoric (s_{ij}) effective stress tensors as $\sigma_{kk}/3$ and $\sqrt{(3/2)s_{ij}s_{ij}} \cdot \cos(3\theta_\sigma)$, respectively, where θ_σ stands for the Lode angle.

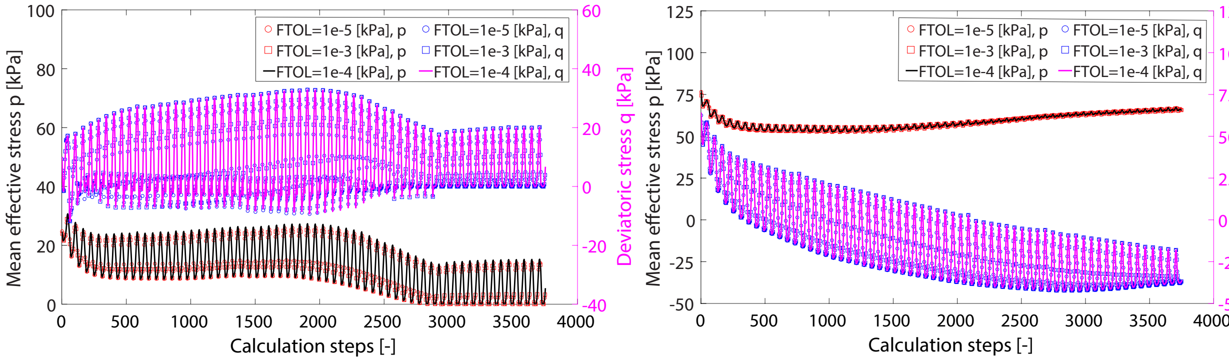

(a) Element B **(b) Element D**

Fig. 19. Influence of $FTOL$ (tolerance for the yielding test) on stress integration at elements B and D in Fig. 2 – simulation case L2 in Table 3. Values of mean and deviatoric stress invariants were obtained from the total (σ_{ij}) and deviatoric (s_{ij}) effective stress tensors as $\sigma_{kk}/3$ and $\sqrt{(3/2)s_{ij}s_{ij}} \cdot \cos(3\theta_\sigma)$, respectively, where θ_σ stands for the Lode angle.

accounting for cyclic mobility effects. *Soil Dynamics and Earthquake Engineering* **97**, 439–453.

Been, K. & Jefferies, M. G. (1985). A state parameter for sands. *Géotechnique* **35**, No. 2, 99–112.

Bhattacharya, S. (2019). *Design of foundations for offshore wind turbines*. Wiley Online Library.

Bolton, M. (1986). Strength and dilatancy of sands. *Geotechnique* **36**, No. 1, 65–78.

Borja, R. I. & Amies, A. P. (1994). Multiaxial cyclic plasticity model for clays. *Journal of geotechnical engineering* **120**, No. 6, 1051–1070.

Cerfontaine, B., Dieudonné, A.-C., Radu, J.-P., Collin, F. & Charlier, R. (2015). 3D zero-thickness coupled interface finite element: Formulation and application. *Computers and Geotechnics* **69**, 124–140.

Chancham, C., Waewsak, J. & Gagnon, Y. (2017). Offshore wind resource assessment and wind power plant optimization in the gulf of thailand. *Energy* **139**, 706–731.

Cheng, X., Diambra, A., Ibraim, E., Liu, H. Y. & Pisanò, F. (2021). 3D FE-informed laboratory soil testing for the design of offshore wind turbine monopiles. *Journal of Marine Science and Engineering* , accepted for publication.

Chong, S.-H. (2017). Numerical simulation of offshore foundations subjected to repetitive loads. *Ocean Engineering* **142**, 470–477.

Corciulo, S., Zanoli, O. & Pisanò, F. (2017). Transient response of offshore wind turbines on monopiles in sand: role of cyclic hydro–mechanical soil behaviour. *Computers and Geotechnics* **83**, 221–238.

Corti, R., Diambra, A., Muir Wood, D., Escribano, D. E. & Nash, D. F. (2016). Memory surface hardening model for granular soils under repeated loading conditions. *Journal of Engineering Mechanics* , 04016102.

Cuéllar, P., Baeßler, M. & Rücker, W. (2009). Ratcheting convective cells of sand grains around offshore piles under cyclic lateral loads. *Granular Matter* **11**, No. 6, 379.

Cuéllar, P., Mira, P., Pastor, M., Merodo, J. A. F., Baeßler, M. & Rücker, W. (2014). A numerical model for the transient analysis of offshore foundations under cyclic loading. *Computers and Geotechnics* **59**, 75–86.

Dafalias, Y. F. & Manzari, M. T. (2004). Simple plasticity sand model accounting for fabric change effects. *Journal of Engineering mechanics* **130**, No. 6, 622–634.

Day, R. & Potts, D. (1994). Zero thickness interface elementsnumerical stability and application. *International Journal for numerical and analytical methods in geomechanics* **18**, No. 10, 689–708.

di Prisco, C. & Mortara, G. (2013). A multi-mechanism constitutive model for plastic adaption under cyclic loading. *International Journal for Numerical and Analytical Methods in Geomechanics* **37**, No. 18, 3071–3086.

di Prisco, C. & Pisanò, F. (2011). Seismic response of rigid shallow footings. *European Journal of Environmental and Civil Engineering* **15**, No. sup1, 185–221.

Gao, G. & Meguid, M. (2018). Effect of particle shape on the response of geogrid-reinforced systems: insights from 3D discrete element analysis. *Geotextiles and Geomembranes* **46**, No. 6, 685–698.

Ghofrani, A. & Arduino, P. (2018). Prediction of leap centrifuge test results using a pressure-dependent bounding surface constitutive model. *Soil Dynamics and Earthquake Engineering* **113**, 758–770.

Griffiths, D. (1985). Numerical modelling of interfaces using conventional finite elements. In *International conference on numerical methods in geomechanics*, pp. 837–844.

Heins, E., Bienen, B., Randolph, M. F. & Grabe, J. (2020). Effect of installation method on static and dynamic load test response for piles in sand. *International Journal of Physical Modelling in Geotechnics* **20**, No. 1, 1–23.

Houlsby, G. (2016). Interactions in offshore foundation design. *Géotechnique* **66**, No. 10.

Houlsby, G., Abadie, C., Beuckelaers, W. & Byrne, B. (2017). A model for nonlinear hysteretic and ratcheting behaviour. *International Journal of Solids and Structures* **120**, 67–80.

Jostad, H., Grimstad, G., Andersen, K., Saue, M., Shin, Y. & You, D. (2014). A FE procedure for foundation design of offshore structures–applied to study a potential owt monopile foundation in the korean western sea. *Geotechnical Engineering Journal of the SEAGS & AGSSEA* **45**, No. 4, 63–72.

Jostad, H. P., Dahl, B. M., Page, A., Sivasithamparam, N. & Sturm, H. (2020). Evaluation of soil models for improved design of offshore wind turbine foundations in dense sand. *Géotechnique* , 1–18.

Kementzetzidis, E., Corciulo, S., Versteijlen, W. G. & Pisanò, F. (2019). Geotechnical aspects of offshore wind turbine dynamics from 3d non-linear soil-structure simulations. *Soil Dynamics and Earthquake Engineering* **120**, 181–199.

Kementzetzidis, E., Metrikine, A. V., Versteijlen, W. G. & Pisanò, F. (2020). Frequency effects in the dynamic lateral stiffness of monopiles in sand: insight from field tests and 3D FE modelling. *Géotechnique* , Ahead of print.

Kementzetzidis, E., Versteijlen, W. G., Nernheim, A. & Pisanò, F. (2018). 3d fe dynamic modelling of offshore wind turbines in sand: natural frequency evolution in the pre–to after-storm transition. In *Proceedings of the 9th european conference on numerical methods in geotechnical engineering (NUMGE 2018), june 25-27, 2018, porto, Portugal*, CRC Press, pp. 1477–1484.

Klinkvort, R. T. (2013). *Centrifuge modelling of drained lateral pile-soil response: Application for offshore wind turbine support structures*. Ph.D. thesis, Technical University of Denmark.

LeBlanc, C., Houlsby, G. T. & Byrne, B. W. (2010). Response of stiff piles in sand to long-term cyclic lateral loading. *Géotechnique* **60**, No. 2, 79–90.

Li, X. & Dafalias, Y. F. (2000). Dilatancy for cohesionless soils. *Geotechnique* **50**, No. 4, 449–460.

Liu, H. Y. (2020). *Constitutive modelling of cyclic sand behaviour for offshore foundations*. Ph.D. thesis, Delft University of Technology.

Liu, H. Y., Abell, J., Diambra, A. & Pisano, F. (2019a). Capturing cyclic mobility and preloading effects in sand using a memory-surface hardening model. In *Proc. of 7th Int. Conf. on Earthquake Geotechnical Engineering (7ICEGE)*, pp. 17–20.

Liu, H. Y., Abell, J. A., Diambra, A. & Pisanò, F. (2019b). Modelling the cyclic ratcheting of sands through memory-enhanced bounding surface plasticity. *Géotechnique* **69**, No. 9, 783–800.

Liu, H. Y., Diambra, A., Abell, J. A. & Pisanò, F. (2020). Memory-enhanced plasticity modeling of sand behavior under undrained cyclic loading. *Journal of Geotechnical and Geoenvironmental Engineering* **146**, No. 11, 04020122.

Liu, H. Y. & Pisanò, F. (2019). Prediction of oedometer terminal densities through a memory-enhanced cyclic model for sand. *Géotechnique Letters* **9**, No. 2, 81–88, doi:10.1680/jgele.18.00187.

Liu, H. Y., Zygounas, F., Diambra, A. & Pisanò, F. (2018). Enhanced plasticity modelling of high-cyclic ratcheting and pore pressure accumulation in sands. In *Numerical Methods in Geotechnical Engineering IX, Volume 1: Proceedings of the 9th European Conference on Numerical Methods in Geotechnical Engineering (NUMGE 2018), June 25-27, 2018, Porto, Portugal*, CRC Press, p. 87.

Manzari, M. T. & Dafalias, Y. F. (1997). A critical state two-surface plasticity model for sands. *Géotechnique* **47**, No. 2, 255–272.

Mattar, C. & Borvarán, D. (2016). Offshore wind power simulation by using WRF in the central coast of chile. *Renewable Energy* **94**, 22–31.

McAdam, R. A., Byrne, B. W., Houlsby, G. T., Beuckelaers, W. J., Burd, H. J., Gavin, K. G., Igoe, D. J., Jardine, R. J., Martin, C. M., Muir Wood, A. *et al.* (2019). Monotonic laterally loaded pile testing in a dense marine sand at dunkirk. *Géotechnique* , Ahead of print.

McGann, C. R., Arduino, P. & Mackenzie-Helnwein, P. (2015). A stabilized single-point finite element formulation for three-dimensional dynamic analysis of saturated soils. *Computers and Geotechnics* **66**, 126–141.

McKenna, F. (2011). Opensees: a framework for earthquake engineering simulation. *Computing in Science & Engineering* **13**, No. 4, 58–66.

Metrikine, A., Tsouvalas, A., Segeren, M., Elkadi, A., Tehrani, F., Gómez, S., Atkinson, R., Pisanò, F., Kementzetzidis, E., Tsetas, A., Molenkamp, T., van Beek, K. & P, D. (2020). Gdp: a new technology for gentle driving of (mono)piles. In *Frontiers in Offshore Geotechnics IV: Proceedings of the 4th International Symposium on Frontiers in Offshore Geotechnics (ISFOG 2021)*.

Nicolai, G. & Ibsen, L. B. (2014). Small-scale testing of cyclic laterally loaded monopiles in dense saturated sand. *Journal of Ocean and Wind Energy* **1**, No. 4, 240–245.

Niemunis, A., Wichtmann, T. & Triantafyllidis, T. (2005). A high-cycle accumulation model for sand. *Computers and geotechnics* **32**, No. 4, 245–263.

Page, A. M., Klinkvort, R. T., Bayton, S., Zhang, Y. & Jostad, H. P. (2020). A procedure for predicting the permanent rotation of monopiles in sand supporting offshore wind turbines. *Marine Structures* **75**, 102813.

Page, A. M., Næss, V., De Vaal, J. B., Eiksund, G. R. & Nygaard, T. A. (2019). Impact of foundation modelling in offshore wind turbines: Comparison between simulations and field data. *Marine Structures* **64**, 379–400.

Park, J. & Santamarina, J. (2019). Sand response to a large number of loading cycles under zero-lateral-strain conditions: evolution of void ratio and small-strain stiffness. *Géotechnique* **69**, No. 6, 501–513.

Pisanò, F. (2019). Input of advanced geotechnical modelling to the design of offshore wind turbine foundations. In *Proceedings of the 17th European Conference on Soil Mechanics and Geotechnical Engineering (ECSMGE 2019)*, International Society of Soil

Mechanics and Geotechnical Engineering.

Richards, I., Bransby, M., Byrne, B., Gaudin, C. & Houlsby, G. (2021). Effect of stress level on response of model monopile to cyclic lateral loading in sand. *Journal of Geotechnical and Geoenvironmental Engineering* **147**, No. 3, 04021002.

Richards, I. A. (2019). *Monopile foundations under complex cyclic lateral loading*. Ph.D. thesis, University of Oxford.

Richards, I. A., Byrne, B. W. & Houlsby, G. T. (2019). Monopile rotation under complex cyclic lateral loading in sand. *Géotechnique* , Ahead of print.

Rudolph, C., Bienen, B. & Grabe, J. (2014). Effect of variation of the loading direction on the displacement accumulation of large-diameter piles under cyclic lateral loading in sand. *Canadian Geotechnical Journal* **51**, No. 10, 1196–1206.

Scott, M. H. & Fenves, G. L. (2003). A krylov subspace accelerated newton algorithm. In *2003 ASCE/SEI Structures Congress and Exposition: Engineering Smarter*.

Sheil, B. B. & McCabe, B. A. (2017). Biaxial loading of offshore monopiles: numerical modeling. *International Journal of Geomechanics* **17**, No. 2, 04016050.

Sloan, S. W. (1987). Substepping schemes for the numerical integration of elastoplastic stress–strain relations. *International journal for numerical methods in engineering* **24**, No. 5, 893–911.

Sloan, S. W., Abbo, A. J. & Sheng, D. (2001). Refined explicit integration of elastoplastic models with automatic error control. *Engineering Computations* **18**, No. 1/2, 121–194.

Staubach, P., Machaček, J., Moscoso, M. & Wichtmann, T. (2020). Impact of the installation on the long-term cyclic behaviour of piles in sand: A numerical study. *Soil Dynamics and Earthquake Engineering* **138**, 106223.

Staubach, P. & Wichtmann, T. (2020). Long-term deformations of monopile foundations for offshore wind turbines studied with a high-cycle accumulation model. *Computers and Geotechnics* **124**, 103553.

Taborda, D. M., Zdravković, L., Potts, D. M., Burd, H. J., Byrne, B. W., Gavin, K. G., Houlsby, G. T., Jardine, R. J., Liu, T., Martin, C. M. *et al.* (2019). Finite-element modelling of laterally loaded piles in a dense marine sand at dunkirk. *Géotechnique* , Ahead of print.

Tamagnini, C., Viggiani, G., Chambon, R. & Desrues, J. (2000). Evaluation of different strategies for the integration of hypoplastic constitutive equations: Application to the cloe model. *Mechanics of Cohesive-frictional Materials: An International Journal on Experiments, Modelling and Computation of Materials and Structures* **5**, No. 4, 263–289.

Truong, P., Lehane, B. M., Zania, V. & Klinkvort, R. T. (2019). Empirical approach based on centrifuge testing for cyclic deformations of laterally loaded piles in sand. *Géotechnique* **69**, No. 2, 133–145, doi:10.1680/jgeot.17.P.203.

Tsai, Y.-C., Huang, Y.-F. & Yang, J.-T. (2016). Strategies for the development of offshore wind technology for far-east countries–a point of view from patent analysis. *Renewable and Sustainable Energy Reviews* **60**, 182–194.

Tsuha, C. d. H., Foray, P., Jardine, R., Yang, Z. X., Silva, M. & Rimoy, S. (2012). Behaviour of displacement piles in sand under cyclic axial loading. *Soils and foundations* **52**, No. 3, 393–410.

Wichtmann, T. (2005). *Explicit accumulation model for non-cohesive soils under cyclic loading*. Ph.D. thesis, Inst. für Grundbau und Bodenmechanik Bochum University, Germany.

Wichtmann, T., Triantafyllidis, T., Chrisopoulos, S., Zachert, H. *et al.* (2017). Prediction of long-term deformations of offshore wind power plant foundations using HCA-based engineer-oriented models. *International Journal of Offshore and Polar Engineering* **27**, No. 04, 346–356.